Contents lists available at ScienceDirect

Journal of Power Sources

3D strongly anisotropic intrinsic thermal conductivity of polypropylene separator

Qusai Alahmad [1], Mahya Rahbar [1], Amin Karamati, John Bai, Xinwei Wang [*]

Department of Mechanical Engineering, 271 Applied Science Complex II, Iowa State University, Ames, IA, 50011, USA

HIGHLIGHTS

- Polypropylene (PP) separator has 3D anisotropic intrinsic thermal conductivity (k).
- The k in the parallel direction is 5 times that in the normal direction.
- The k in the thickness direction is less than 60% of that in the normal direction.
- The sample and air in it follow parallel configuration in the thickness direction.
- Anisotropic micro/nanoscale structure of PP separator and anisotropic k of bulk PP.

GRAPHICAL ABSTRACT

ARTICLE INFO

ABSTRACT

In this work, the thermal conductivity in every direction is reported for the first time for the dry separator component made out of polypropylene (PP) that is used in lithium-ion batteries. Herein, a PP separator film is studied dry and in vacuum, as an example of polyolefins separators. These separators are crucial for performance parameters, including cycle life, thermal management, energy and power density, and safety. Hence, a better understanding of the thermal conductivity k in different in-plane directions (parallel and normal direction to the stretching direction in fabrication) as well as the out-of-plane direction is crucial to the overall performance. k of dry PP separator, measured in vacuum, is found four times bigger in the parallel direction (0.217 W·m^{-1}·K^{-1}) than in the normal direction (0.043 W·m^{-1}·K^{-1}), all for the in-plane direction. This strong anisotropy can be explained by the macroscopic and microscopic anisotropic structure and intrinsic anisotropic thermal conductivity of aligned PP. Moreover, the out-of-plane k of the dry PP separator is measured to be 0.036 and 0.025 W·m^{-1}·K^{-1} in the air and vacuum, respectively, suggesting good parallel structure of PP in the thickness direction.

1. Introduction

Lithium-ion batteries (LIBs) are one of the most used and studied storage units in engineering applications. Cathode, anode, electrolyte, and separator are the four basic components of LIBs [1–4]. Knowledge of the thermal characteristics of LIBs components, like thermal conductivity, is pivotal for their performance and safety [5–8]. The separator component is crucial when evaluating performance parameters,

---

* Corresponding author.
  E-mail address: xwang3@iastate.edu (X. Wang).
[1] Equal contribution authors.

including cycle life, thermal management, energy and power density, and safety [9–13]. This thin microporous film facilitates ion flow in the cell and avoids physical contact between the anode and cathode. Microporous films used as separators are required to have a broad range of characteristics [9], such as being homogeneous in thickness, mechanically and dimensionally stable, and with low electrolyte (ionic) resistance. Most LIBs use microporous membranes made of polyolefins, such as polyethylene (PE) and polypropylene (PP), for they provide excellent mechanical properties [9]. Polyolefins have been developed and used extensively in LIBs. The composition can consist of many forms like PE, PP/PE, or PP/PE/PP, mainly because PE has a lower melting point than PP and could work as a shutoff agent in case of battery overheating [14,15]. A more in-depth breakdown of the requirements of LIBs separators are provided in Refs. [9,16], like thickness that is recommended to be < 25 μm, dimensional and chemical stability, and thermal stability.

Furthermore, one element that plays a crucial role in the safe operation of the battery is having good heat distribution of the separator. This can mitigate heat accumulation at high temperatures [10,11]. This leads us to study a significant characteristic in designing a safe battery separator: thermal conductivity [10]. Uniform and stable thermal conductivity is essential to preserve the batteries' mechanical integrity at high temperatures [9] in order to achieve high ion flow and mitigate overheating that could lead to damage or internal short-circuiting. Thermal conductivity was discussed in many previous studies of LIB separators in different directions, out-of-plane or in-plane, and states of either soaked in an electrolyte or dry [17–24]. Table 1 summarizes a breakdown of some of these studies. As shown in Table 1, none of the aforementioned studies addressed the thermal conductivity anisotropy of separators while this characteristic is critical to understanding separators' structure and heat conduction capacity. This study aims to investigate the intrinsic thermal conductivity of separators, and shows that LIB separators have highly anisotropic thermal conductivities. Herein, a PP separator film is studied as an example of polyolefins separators to show the thermal conductivity of LIB separators is very different in the two in-plane directions (parallel and normal directions to the stretching direction in fabrication) as well as the out-of-plane direction, which is explained by detailed anisotropic structure. Two techniques will be used to measure the thermal conductivity, the transient electrothermal (TET) [25] technique for in-plane thermal conductivity measurement, and the differential thermal resistance (DTR) technique [26] for out-of-plane thermal conductivity measurement.

Both techniques were developed, calibrated, and validated by our lab.

2. Experimental section

2.1. Materials

Herein, the Celgard® 2500 separator, with a thickness of 25 μm made from a monolayer microporous membrane of PP, is studied. It is a low-cost and relatively inert polymer made for high-rate and low-temperature applications. It is insoluble in most solvents at room temperature and resistant to extreme pH settings. When soaked in polar solvents such as carbon tetrachloride, it swells. One significant advantage is that no solvent is required for the film's preparation. Four main processes (extrusion, cooling, stretching, and cooling again) are used in this PP film production. First, PP is extruded into films with high melt stress. When cooling, the polymer chains are aligned, which causes the production of lamellar microcrystallites. Then, just below the melting point, the film is stretched by 50–300%. The amorphous phase between the crystallites deforms under stress, forming slit-like holes that make up the Celgard membrane. Finally, the film is tensioned while cooling [27].

2.2. Measurement of in-plane thermal diffusivity

The TET technique is used to measure the in-plane thermal conductivity. The TET technique was first developed by our lab back in 2007 [25]. It has been proven very successful in measuring the thermal diffusivity of fiber- or film-like materials with a high sensitivity (better than 5%). Micro/nanoscale fibers/films of semiconductive, metallic, polymer, and dielectric materials have been measured successfully by using the TET technique [28–32]. A schematic of the TET approach is shown in the inset of Fig. 1(a). In this technique, an abrupt voltage increase is induced by Joule heating using a step DC current. The transient temperature variation over the sample is then used to compute the thermal diffusivity. Due to the sample's high length-to-thickness ratio, it is reasonable to infer that the heat conduction is one-dimensional. In the end, the transient temperature response over the sample and the one-dimensional heat transfer model can be used:

$$\frac{\partial\left(\rho c_{\mathrm{p}} T\right)}{\partial t} = k\frac{\partial^2 T}{\partial x^2} + \dot{q}_0, \tag{1}$$

where ρ is the film's density, c_{p} specific heat, k thermal conductivity, and $\dot{q}_0$ is the sample's electrical heating power per unit volume. This

Table 1
Measured thermal conductivity of different types of separators in different directions and under different conditions.

Separator composition	Separator state under study	Thermal conductivity (W·m⁻¹·K⁻¹)	Direction of study	Thickness	Reference
Polyethylene terephthalate	Dry	0.10 ± 0.04 0.12 ± 0.01 0.12 ± 0.02 0.14 ± 0.03	Out-of-plane	Undetermined by the study	[17]
	Soaked	0.36 ± 0.03 0.36 ± 0.02 0.31 ± 0.02 0.28 ± 0.01			
PP	Dry	0.07 ± 0.01	Out-of-plane	25 μm	[17]
	Soaked	0.14 ± 0.03			
PP/PE/PP	Soaked	0.19 ± 0.03	Out-of-plane In-plane	24 μm	[18]
PP/PE/PP	Soaked	0.43–0.5	Undetermined by the study, but the study compared with out-of-plane references.	20–50 μm	[19]
PP/PE/PP	Soaked	0.35	Out-of-plane	50 μm	[20]
PP/PE/PP	Soaked	0.334	Out-of-plane	Undetermined by the study	[21]
PE	Extracted and dried	0.50 ± 0.03	In-plane	Undetermined by the study	[22]
PP	Soaked	0.34	Out-of-plane	25 μm	[23]
PP	Soaked	0.3344	Out-of-plane	35 μm	[24]
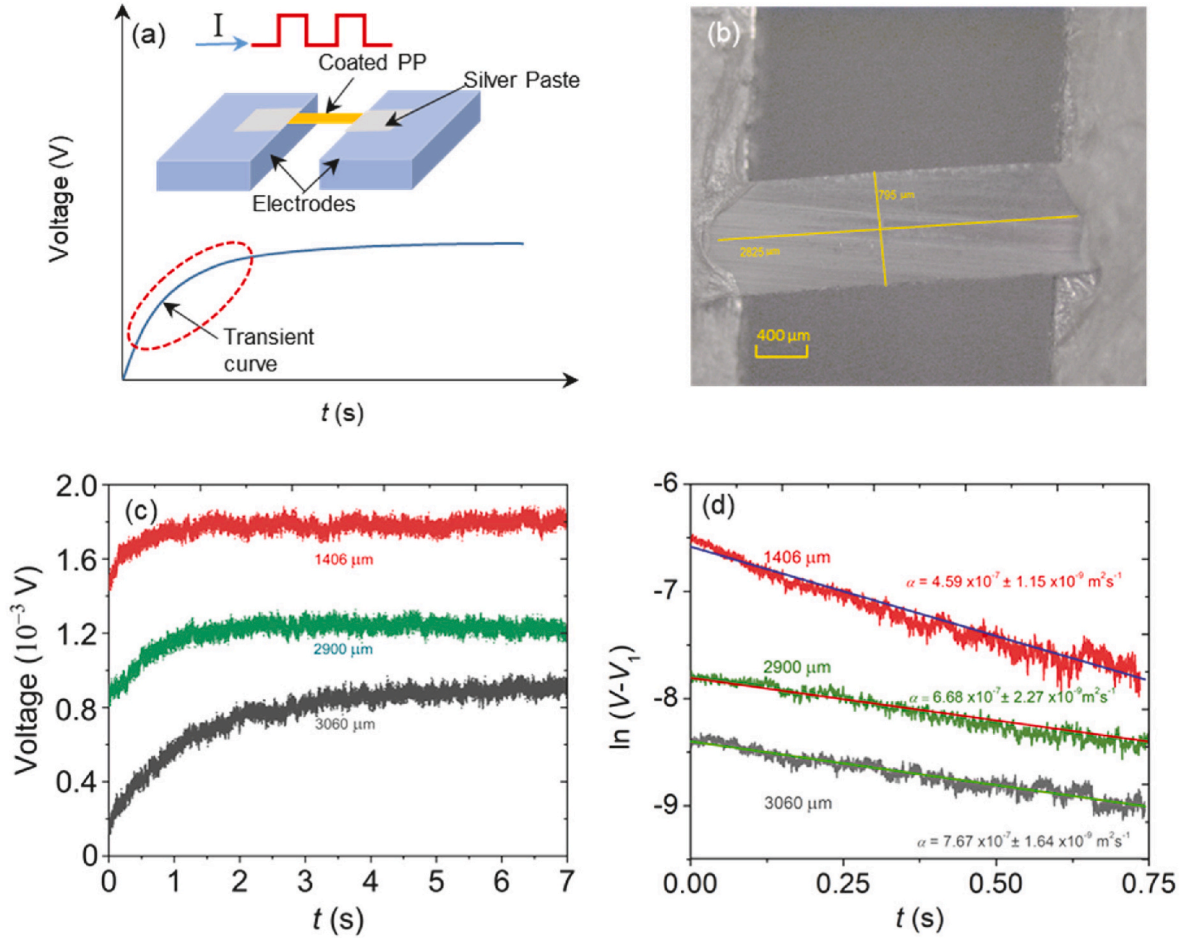
Fig. 1. (a) Schematic illustrating the step current used in the TET measurement and the experimental concept alongside the methodology for determining thermal diffusivity based on the transient curve of the experimental *V-t* signal. (b) A suspended PP sample (parallel direction) coated with iridium for TET measurement. (c) TET signal (experimental data) for samples of different lengths (parallel direction). (d) The natural logarithm of PP TET voltage change (V-V_1) with V_1 as the final steady state voltage (experimental data) for samples of different lengths (parallel direction) along with the data fitting.

problem's initial condition is $T(x) = T_0$ (T_0: ambient temperature). Due to the bulk aluminum (Al) electrode, which the sample is suspended on, being a thermal reservoir, this would lead to $T(x = 0, t) = T(x = L, t) = T_0$. Equation (1) can be solved analytically. By assuming a linear R-T correlation within the moderate temperature rise (ΔT, typically <4 K) of each measurement, the normalized voltage rise $V^*(t) = [V(t) - V_0]/(V_1 - V_0)$ is equal to the normalized temperature rise $T^*(t) = [T(t) - T_0]/(T_1 - T_0)$, where V_0 is the initial voltage, T_1 and V_1 are the voltage and temperature at the final steady state, respectively. The solution can be spelled out as follows [25,28],

$$T^* = \frac{96}{\pi^4} \sum_{m=1}^{\infty} \frac{1 - \exp\left[-(2m-1)^2 \pi^2 \alpha_{eff} t / L^2\right]}{(2m-1)^4}, \quad (2)$$

where α_{eff} is the thermal diffusivity containing the radiation and coating effect, and L is the sample's length.

A new data processing method was introduced by Karamati et al. [33] when the sample experiences a voltage rise (or drop), which reflects the sample's temperature change. After calculating the natural log of this transient voltage change, they discovered that the data series closely matches a line with a coefficient of $b = -\pi^2 \alpha_{eff}/L^2$. The relation can be expressed as $\ln|V - V_1| = a - bt$. Thus, it is feasible to determine the fitting uncertainty by successfully utilizing the linear fitting rather than the more common nonlinear raw data fitting. The aforementioned method is used in this study for data processing to determine α_{eff}. Please note here the absolute temperature rise is not needed since the

temperature rise is proportional to the voltage rise. What is needed in data reduction is the relative/normalized temperature change. Nevertheless, during the TET test, the temperature rise is commonly less than 10 K when the voltage is increased by 3% or less [34]. In this work, for this TET measurement the temperature rise is less than 5 K. Knowing the thermal expansion coefficient (α_{exp}) of pure PP as $14.8 \times 10^{-6}/°C$ at room temperature [35], taking the sample in Fig. 1(b) with a length of 2825 μm, and solving for the change in length as: $\Delta L = \alpha_{exp} L \Delta T$, where L is the sample's length, and ΔT is the temperature rise, ΔL is obtained as 0.2 μm when taking ΔT as 5 K. So it is safe to neglect the thermal expansion effect on the sample, as well as any stress or tension caused by it.

2.3. Measurement of out-of-plane thermal conductivity

The out-of-plane thermal conductivity of the dry PP sample is measured in the air and vacuum. Fig. 2(a) and (b) show the physical principles of this measurement, respectively. In order to measure the out-of-plane thermal conductivity of the sample in the air, the DTR technique, first developed by our lab, is used. It has been successfully validated by measuring the out-of-plane thermal conductivity of two acrylic samples with different thickness in our previous work [26]. As shown in Fig. 2(a), the sample is coated with a black tape and attached to an Al substrate with another double side black tape. A 1550 nm laser irradiates the top surface of the black tape, which causes the temperature of the sample to increase. An infrared camera measures the surface
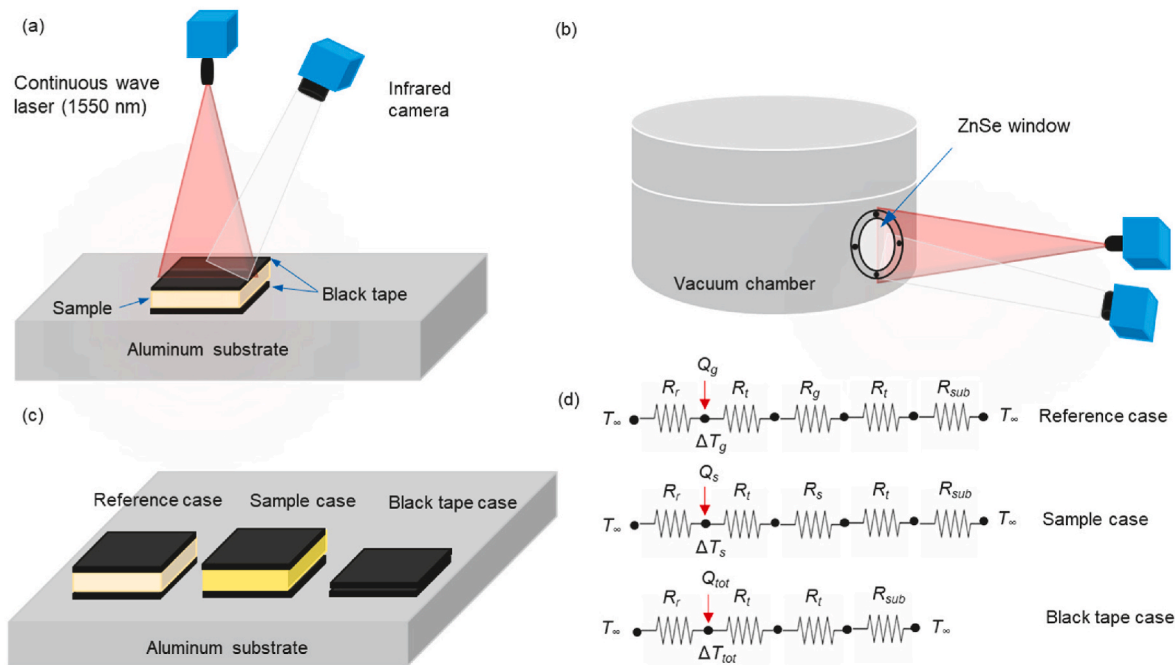
Fig. 2. (a) Physical principles of the DTR technique for out-of-plane thermal conductivity measurement in the air, and (b) in the vacuum. (c) Three configurations used in this measurement. (d) Thermal resistance circuits for each configuration with the laser heating location. (Not to scale.)

temperature rise. Note that this temperate rise depends on the absorbed laser power (Q), the thermal resistance of the sample (R_s), the thermal resistance of the two black tapes (R_t), the thermal resistance of radiation-convection (R_{rc}) on the top of the sample, and the thermal resistance of the substrate system (R_{sub}), as shown in Fig. 2(d). The laser spot is large enough to cover the entire sample, and irradiating laser energy is measured by a power meter precisely. Also, the reason for using a top black tape is to maximize the laser absorption with minimum reflection. Two other configurations, including the reference case and the black tape, as shown in Fig. 2(c), were designed to determine the unknown thermal resistances of the black tape, Al substrate, convection and radiation. The black tape is exactly the same as those used in the sample configuration.

Three differential equations corresponding to each thermal circuit provided in Fig. 2(d) can be solved simultaneously to obtain the sample's thermal conductivity k. More details of experiment, including differential equations can be found in the supplemental document. We also extended the DTR technique to the vacuum chamber ($P\sim20$ μbar) measurement, as shown in Fig. 2(b), to eliminate the convection resistance and the effect of air inside the porous sample. Above mentioned three cases have been placed in the vacuum, and the same procedure is conducted. A ZnSe window on the vacuum chamber allows the laser to come in. ZnSe is ~60–80% transparent for the 1550 nm wavelength laser depending on the thickness and temperature [36,37]. Here we directly measure the laser power inside the vacuum, so the transparency of ZnSe window has been applied automatically. In addition, since we are interested in temperature rise, the transparency of ZnSe window affects the measurements very little and the effect is calibrated.

3. Results

3.1. Structure characterization

Fig. 3(a) depicts the scanning electron microscopy (SEM) results of the PP sample. As seen in the inset, the material is stretched, and the pores are aligned in the parallel direction (the stretching direction in fabrication). It is also noticeable that the macroscopic structure of the PP film is anisotropic. The pores have a quasi-elliptical shape with a minor

axis length that can go up to ~200 nm. The threads forming that quasi-elliptical shape can have a diameter up to ~50 nm.

Moreover, as shown in Fig. 3(b), the film's Raman spectrum matches the isotactic polypropylene's Raman spectrum. The peaks between 2800 and 3000 cm^{-1} could be ascribed to stretching vibrations of C-H of the PP membrane. In Fig. 3(c), the XRD results tell that the material is crystalline with some amorphous structure within the film. To calculate the crystallite size τ, the Scherrer equation is used [38]:

$$\tau = \frac{K\lambda}{\beta\cos\theta},$$ (3)

where K is shape factor, λ x-ray wavelength, β full width at half maximum of peaks (FWHM) in radian located at any 2θ, and θ the Bragg angle. Solving Eq. (3), and taking the peaks in the first three planes (110), (040), and (130), the crystallite sizes are found to be 10.2, 12.1, and 10.6 nm, respectively, indicating the sample has quite sphere-like crystalline grains. Please note that K and λ are taking as 0.89 and 1.5432 Å, respectively.

Fig. 3(d) illustrates the heat capacity (c_p) results based on differential scanning calorimetry (DSC) done on the film. The temperature ranges from −50 °C up to 150 °C. A linear behavior can be observed up to around 140 °C, and then the curve starts an exponential growth toward its melting temperature of approximate 160 °C [39]. The heat capacity around the room temperature is found to be 1.45 J·g^{-1}·K^{-1}, which is used in this study for thermal conductivity calculation. Previous studies [23,24] used a c_p of 1.978 J·g^{-1}·K^{-1} for their soaked PP separators. Furthermore, the density (ρ_{porous}) measured for our PP film is 0.42 g·cm^{-3}. The porosity of the PP film is calculated as $\varphi = 1 - \rho_{porous}/\rho_{bulk}$, where the bulk PP's density (ρ_{bulk}) is 0.907 g·cm^{-3} [40]. The porosity is calculated as 54%, which is very similar to the value of 55% documented by the manufacturer.

3.2. In-plane effective thermal conductivity

In our measurement, the sample is coated with an Iridium (Ir) film to make it electrically conductive, and is connected to two Al electrodes using silver paste to ensure sound thermal and electrical contacts [as
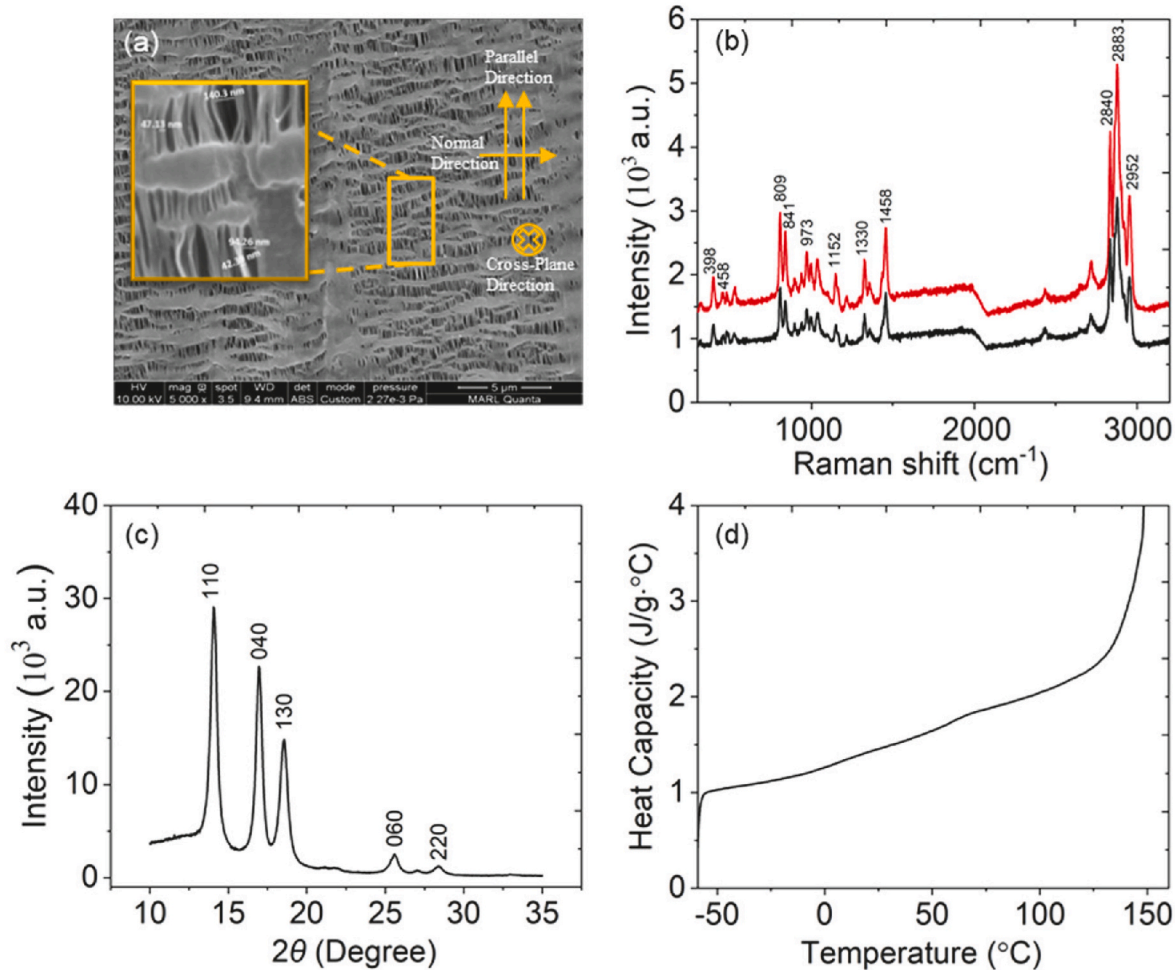
Fig. 3. (a) SEM image of PP studied in this work. The inset shows details of pores within the separator. (b) Raman spectra for the PP at two selected locations. (c) XRD patterns of the PP film. (d) DSC measurement of the specific heat of the PP film from −50 to 150 °C.

shown in Fig. 1(a)]. Fig. 1(b) shows one of the studied samples with a length 2825 μm and width of 795 μm. In TET measurements, the sample is housed in a vacuum chamber of 7 μBar pressure to make the convection effect negligible. Fig. 1(c) shows the raw TET data measured for three samples in the parallel direction, and Fig. 1(d) shows the data fitting process of these samples to determine α_{eff}. It is evident sound linear fitting can be obtained with a relative fitting uncertainty in the range of 0.25%. Fig. 1(d) shows longer samples have larger effective thermal diffusivities. This is due to the radiation effect, and will be analyzed in the next section.

3.3. Effect of radiation on in-plane thermal conductivity measurement

After α_{eff} is determined, the intrinsic α value is determined by taking out the radiation and Ir coating contributions, which have been discussed previously in Refs. [28,41]. Considering the radiation effect, we have,

$$\alpha_{eff} = \alpha_{eff,Ir} + \frac{8\varepsilon\sigma T^3 L^2}{\pi^2 D\rho c_p},\qquad(4)$$

where $\alpha_{eff,Ir}$ is the effective thermal diffusivity carrying the coating's effect, ε is the surface emissivity, σ the Stefan-Boltzmann constant, D sample's thickness, and T the sample's temperature. From Eq. (4), it is evident that α_{eff} has a linear relationship with the sample's squared length, where the slope is $8\varepsilon\sigma T^3/(\pi^2 D\rho c_p)$. In order to subtract the radiation effect, multiple samples of different lengths are measured. Please

note for all these samples, the Ir coating thickness is 10 nm during TET measurement. This is to ensure they have the same effect from the coating on thermal diffusivity measurement. The coating's effect will be subtracted in the next section. Fig. 4(a) shows the results for the parallel and normal direction measurement. Excellent linear relationship is observed between α_{eff} and L^2. The y-axis intercept in Fig. 4(a) is the value of α_{eff} without radiation: $\alpha_{eff,Ir}$. This is the thermal diffusivity isolated from the radiation effect but still carrying the Ir coating effect. $\alpha_{eff,Ir}$ is found to be 3.65×10^{-7} and 0.85×10^{-7} m²·s⁻¹ for the parallel and normal directions, respectively. The fitting uncertainty for the $\alpha_{eff,Ir}$ intercept is 2.0% and 5.6% for the parallel and normal directions, respectively. Using the relation between thermal diffusivity and thermal conductivity [42] where $k = \alpha \cdot \rho c_p$, the thermal conductivities ($k_{eff,Ir}$) of the PP film directions are determined to be 0.222 W·m⁻¹·K⁻¹ with an uncertainty of 2.8% in the parallel, and 0.052 W·m⁻¹·K⁻¹ with an uncertainty of 6.0% in the normal direction.

Simultaneously, the effective emissivity of the PP film ε can be calculated from $8\varepsilon\sigma T^3/(\pi^2 D\rho c_p)$, which is the slope of the two lines in Fig. 4(a). The slopes are found as 0.04 s⁻¹ in the parallel direction and 0.041 s⁻¹ in the normal direction. Knowing the temperature (295 K), thickness (25 μm), density and heat capacity we can solve for the emissivity in Eq. (4), which is found as 0.52 with an uncertainty of 4.3% for the samples in the parallel direction, and 0.53 with an uncertainty of 6.6% for the samples in the normal direction. The surface emissivity of PP was previously found to be 0.965 by Franz et al. [43]. The difference between this value and our value is caused mainly by two things. First,
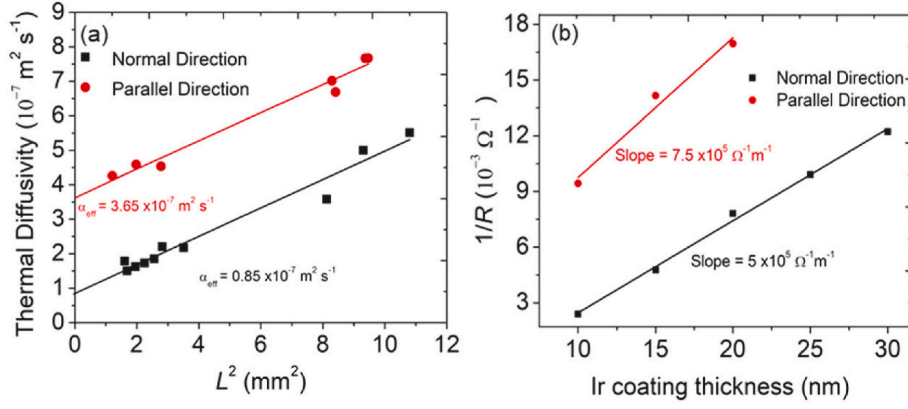
Fig. 4. (a) Effective thermal diffusivity of PP samples of different lengths in parallel and normal directions against the squared length, highlighting the *y*-intercept. (b) Two samples in each direction, showing their inverse of resistance changing linearly with the increment of the coating thickness.

the Ir coating causes a reduction in the emissivity as Ir has a lower emissivity than PP. Second, the radiation effect $8\varepsilon\sigma T^3/(\pi^2 D\rho c_p)$ is based on an assumption that the environment is large and can be treated as a blackbody. This is true for the top side of the sample which faces the inside the vacuum chamber under TET measurement. However, the sample's back side faces the aluminum-base electrodes. These Al bases have a low emissivity (0.04 at 300 K) [44], and are not blackbody. This will reduces the radiation exchange with the sample, hereby resulting in a lower effective surface emissivity of the sample when $8\varepsilon\sigma T^3/(\pi^2 D\rho c_p)$ is used to calculate the radiation heat loss from the surface.

3.4. Effect of iridium-coating on in-plane thermal conductivity measurement

In this section, the process of subtracting the Ir coating effect will be discussed in order to obtain k_s (the sample's real thermal conductivity) isolated from both radiation and coating effects. First of all, we measure the electrical conductivity of the coating. Then the Wiedemann-Franz law is used to calculate the thermal conductivity of the coating. Finally, the coating's contribution to $k_{eff,Ir}$ is calculated. To begin with, two samples cut along the parallel and normal directions are coated with Ir layer for several times. The sample in the parallel direction has a length of 1740 μm and width of 921 μm, and the sample in the normal direction has a length of 3685 μm and width of 628 μm. After each coating thickness increment, the electrical resistance is measured. Fig. 4 (b) shows the relationship between the coating's electrical conductance ($=1/R$) and the coating thickness. We can relate the electrical conductance to the electrical conductivity (σ_e) of the coating as [29,45],

$$R^{-1} = \frac{A\sigma_e}{L} = \frac{D\delta_c \sigma_e}{L}, \tag{5}$$

where σ_e is the electrical conductivity, δ_c the total thickness of the Ir coating on top of the PP film. As can be seen from Fig. 4(b), the slope values were found to be $7.5 \times 10^5\ \Omega^{-1}\cdot\text{m}^{-1}$ and $5 \times 10^5\ \Omega^{-1}\cdot\text{m}^{-1}$ in the parallel and normal directions, respectively. σ_e is obtained from the slope ($D\sigma_e/L$) as $1.45 \times 10^6\ \Omega^{-1}\cdot\text{m}^{-1}$ with an uncertainty of 8.8%, and $3 \times 10^6\ \Omega^{-1}\cdot\text{m}^{-1}$ with an uncertainty of 2.5% in the parallel and normal directions, respectively. From the Wiedemann-Franz law, where a metal's electronic contribution to its thermal and electrical conductivities is correlated with its temperature [46] as,

$$\frac{k_c}{\sigma_e} = L_{\text{Lorenz}} T, \tag{6}$$

where k_c is the thermal conductivity of Ir. The Lorenz number L_{Lorenz} is taken as $2.5 \times 10^{-8}\ \text{W}\cdot\Omega\cdot\text{K}^{-2}$ which is for our Ir coating at room temperature, and has been validated broadly [47]. We can calculate k_c to be

10.5 $\text{W}\cdot\text{m}^{-1}\cdot\text{K}^{-1}$ with an uncertainty of 8.8% for the sample in the parallel direction and 21.8 $\text{W}\cdot\text{m}^{-1}\cdot\text{K}^{-1}$ with an uncertainty of 2.5% in the normal direction. As can be seen here, the Ir coating's thermal conductivities in the two directions are quite different, reflecting the anisotropic nature of the separator's structure. Finally, we can relate the thermal conductivities of the coating and the PP film as,

$$k_{eff,Ir}(\delta_c + D) = k_c\delta_c + k_s D, \tag{7}$$

where k_s is the sample's real conductivity without the effect of radiation and Ir coating. Knowing the coating thickness (10 nm) and the sample thickness (25 μm), k_s is found to be 0.217 and 0.043 $\text{W}\cdot\text{m}^{-1}\cdot\text{K}^{-1}$ in the parallel and normal directions, respectively. The parallel direction's thermal conductivity is four times bigger than that in the normal direction, uncovering very strong anisotropy.

For the in-plane thermal conductivity in the parallel direction, the measurement uncertainties of the sample thickness, coating thickness, density, the fitting when subtracting the radiation effect, and the uncertainty of coating's thermal conductivity are 2.0%, 5.0%, 2.0%, 2.8%, and 8.8%, respectively, resulting the thermal conductivity uncertainty to be 2.9%. Likewise, for the normal direction, measurement uncertainties of the sample thickness, coating thickness, density, the fitting when subtracting the radiation effect, and the uncertainty of coating's thermal conductivity are 2%, 5%, 2.0%, 6.0%, and 2.5%, respectively, resulting the thermal conductivity uncertainty to be 7.0%.

Due to the complicated structure of the PP film shown in Fig. 3(a), the above anisotropy in thermal conductivity is hard to explain quantitatively, but can still be interpreted based on the anisotropy in macroscopic structure and intrinsic thermal conductivity. As shown in Fig. 3(a), during stretching, pores form in the film, and the PP is broken into many tiny fibers connected by some thick perpendicular structures. Such structure will favor more heat transfer in the parallel direction than the normal direction. As for the anisotropy in thermal conductivity, during stretching, the lamellae in the semicrystal are aligned in the parallel direction, making this direction having a higher thermal conductivity. To put this into perspective, the thermal conductivity of bulk and extruded semicrystalline PP studied by Choy and Greig [40] is compared here. For isotropic PP with 65% crystallinity at room temperature, the thermal conductivity is measured as 0.23 $\text{W}\cdot\text{m}^{-1}\cdot\text{K}^{-1}$. For extruded semicrystalline PP, the thermal conductivity becomes very anisotropic. For instance, for PP extruded (62% crystallinity) with a deformation ratio of 10.5 (the ratio between the cross sectional area of the extrude before and after deformation), at 100 K the thermal conductivity is 0.78 and 0.12 $\text{W}\cdot\text{m}^{-1}\cdot\text{K}^{-1}$ in the direction parallel and normal to the extruding direction (higher temperature data is not available). This is because the lamellae are more aligned in the extruding direction. For our PP separator, because of the stretching, it is

expected the intrinsic thermal conductivity in the parallel direction will be much higher (a few-fold) than that in the normal direction. This will contribute to the observed thermal conductivity anisotropy here.

3.5. Out-of-plane thermal conductivity

Experimental details for both air and vacuum cases are summarized in Table 2. It should be noted that T_1 and T_2 represent the temperature of configurations before and after laser irradiation, and ΔT is the temperature rise caused by laser irradiation. The sample's thermal conductivity is determined to be 0.036 and 0.025 W·m^{-1}·K^{-1} in air and vacuum, respectively.

As there is negligible air in the vacuum during the experiment, it is reasonable that the thermal conductivity decreases in the vacuum. The porosity level of the sample is 54%, and air is a poor conductive material with a thermal conductivity of 0.026 W·m^{-1}·K^{-1} at RT [44]. Under the case that the air and PP are parallel with the heat transfer direction (here the thickness direction), the decrease in thermal conductivity in vacuum can be estimated as $\varphi \times k_{air} = 0.54 \times 0.026 = 0.014$ W·m^{-1}·K^{-1}. Our results show the thermal conductivity has been decreased by 0.011 W·m^{-1}·K^{-1} from air to vacuum, which is very close to this estimated value, indicating that the air and PP are quite following a parallel configuration in the thickness direction. This is more understandable since holes form during stretching and they run through the thickness direction to facilitate ion flow in LIB operation. Note this estimation gives the lower bound of air's effect on the effective thermal conductivity. The slight difference could be due to the fact that the air and PP are not perfectly aligned in the thickness direction, which is true in our case [shown in Fig. 3(a)]. There is radiation exchange among PP pore walls. The equivalent thermal conductivity can be estimated as $k_r = 4\varepsilon\sigma T^3\Lambda$ with Λ as the characteristic pore size in the heat transfer direction. At 300 K and with an emissivity of 1 and at the upper limit of Λ as 1 μm, k_r is estimated to be 6.12×10^{-6} W·m^{-1}·K^{-1}, which is very negligible compared with that of air. If we take the parallel configuration, and use the thermal conductivity measured under vacuum, the intrinsic thermal conductivity of bulk PP in the thickness direction can be estimated to be $k_{i,out} = k_{out}/(1 - \varphi) = 0.054$ W·m^{-1}·K^{-1}. A large difference is observed between our results and those of Richter et al. for dry PP [17], as it is reported in Table 3. This is mainly due to the difference in sample structure. Our sample has a porosity of 54%, while their sample has a porosity of 41%. Having more air in our sample will result in a lower thermal conductivity. In the out-of-plane thermal conductivity in air experiment, the measurement uncertainty of the thickness, area, temperature rise, and laser power are 1.8%, 0.2%, 0.1%, and 0.4%, respectively, resulting the thermal conductivity uncertainty to be 1.8%. Similarly, the measurement uncertainty in the vacuum of the thickness, area, temperature rise, and laser power were 1.8%, 0.2%, 0.1%, and 0.4%, respectively, resulting the thermal conductivity uncertainty to be 1.8%. Note that more details of uncertainty calculation

Table 2
Experimental data for measuring the out-of-plane thermal conductivity of PP separator in the air and vacuum.

Experiment data	Fused glass	Tape (2 layers)	Sample
Length [mm]	8.08	7.85	7.70
Width [mm]	8.20	7.90	7.68
Thickness [mm]	1.59	0.66	0.028
Air			
T_1 [°C]	23.4	23.2	22.9
T_2 [°C]	30.2	27.6	28.8
ΔT [°C]	6.8	4.4	5.9
Q [mW]	221	240	197
Vacuum			
T_1 [°C]	23.3	23.2	23.5
T_2 [°C]	31.5	28.4	29.3
ΔT [°C]	8.2	5.2	5.8
Q [mW]	246	222	157

Table 3
Comparison of out-of-plane k between the current and previous studies (all samples are of 25 μm thickness).

Separator composition	Separator state under study	Thermal conductivity (W·m^{-1}·K^{-1})	Direction of study	Reference
PP	Dry	0.07 ± 0.01	Out-of-plane	[17]
	Soaked	0.14 ± 0.03		
PP	Soaked	0.34	Out-of-plane	[23]
PP	Soaked	0.3344	Out-of-plane	[24]
PP	Dry	0.036	Out-of-plane (air)	Current study
		0.025	Out-of-plane (vacuum)	

are given in the supplemental document.

4. Conclusion

Herein, the thermal conductivity in every direction was reported for the first time for the dry separator component made out of polypropylene (PP) that is used in lithium-ion batteries. A PP separator film was studied dry and in vacuum, as an example of polyolefins separators. Two techniques were implemented in this study to measure the thermal conductivity: the TET technique for in-plane thermal conductivity measurement, and the DTR technique for out-of-plane thermal conductivity measurement. The intrinsic thermal conductivity of PP separators showed a very anisotropic behavior, stronger than the soaked separators where the holes of the material are filled with electrolyte, which make the anisotropic behavior obscure. First, the in-plane thermal conductivity was obtained in a vacuum, and after subtracting the radiation and Ir coating effects, the material showed two different thermal conductivities, where the parallel direction has a thermal conductivity four times bigger than that of the normal direction, a conclusion that was never discussed previously. Moreover, the separator was studied in the out-of-plane direction in both vacuum and air to show the intrinsic thermal conductivity in that direction. Overall, under vacuum condition, our PP separator was measured to have thermal conductivities of 0.217, 0.043, and 0.025 W·m^{-1}·K^{-1} in the in-plane parallel, normal, and out-of-plane directions. This uncovers remarkably strong anisotropy, and can be explained by the anisotropic macroscopic structure and anisotropic intrinsic thermal conductivity. The material showed a lower conductivity under vacuum than air. This difference was quite close to the estimation based on a model of parallel structure in the thickness direction, suggesting the pores run vertically all the way through the thickness.

CRediT authorship contribution statement

Qusai Alahmad: conducted experiments and, Formal analysis, on in-plane thermal conductivity measurement, and. **Mahya Rahbar:** conducted experiments and, Formal analysis, on out-of-plane thermal conductivity measurement. **Amin Karamati:** conducted structure characterization and, Formal analysis. **John Bai:** conducted structure characterization and, Formal analysis. **Xinwei Wang:** conducted project management, conceived the research idea, and conducted result, Formal analysis, and physics interpretation. All authors contributed to paper writing and editing.

Declaration of competing interest

The authors declare the following financial interests/personal relationships which may be considered as potential competing interests: Xinwei Wang reports financial support was provided by National

Science Foundation.

Data availability

Data will be made available on request.

Acknowledgement

Appendix A. Supplementary data

Supplementary data to this article can be found online at https://doi.org/10.1016/j.jpowsour.2023.233377.

References

[1] M. Li, J. Lu, Z. Chen, K. Amine, 30 Years of lithium-ion batteries, Adv. Mater. 30 (2018), 1800561.

[2] M. Yoshio, R.J. Brodd, A. Kozawa, Lithium-ion Batteries, 1, Springer, 2009.

[3] G.E. Blomgren, The development and future of lithium ion batteries, J. Electrochem. Soc. 164 (2016) A5019.

[4] J. Xie, Y.-C. Lu, A retrospective on lithium-ion batteries, Nat. Commun. 11 (2020) 2499.

[5] H. Li, A. Saini, C. Liu, J. Yang, Y. Wang, T. Yang, C. Pan, L. Chen, H. Jiang, Electrochemical and thermal characteristics of prismatic lithium-ion battery based on a three-dimensional electrochemical-thermal coupled model, J. Energy Storage 42 (2021), 102976.

[6] X. Tang, Y. Wang, C. Zou, K. Yao, Y. Xia, F. Gao, A novel framework for Lithium-ion battery modeling considering uncertainties of temperature and aging, Energy Convers. Manag. 180 (2019) 162–170.

[7] F. Bai, M. Chen, W. Song, Q. Yu, Y. Li, Z. Feng, Y. Ding, Investigation of thermal management for lithium-ion pouch battery module based on phase change slurry and mini channel cooling plate, Energy 167 (2019) 561–574.

[8] S. Wang, P. Ren, P. Takyi-Aninakwa, S. Jin, C. Fernandez, A critical review of improved deep convolutional neural network for multi-timescale state prediction of lithium-ion batteries, Energies 15 (2022) 5053.

[9] P. Arora, Z. Zhang, Battery separators, Chem. Rev. 104 (2004) 4419–4462.

[10] J. Chen, X. Huang, B. Sun, P. Jiang, Highly thermally conductive yet electrically insulating polymer/boron nitride nanosheets nanocomposite films for improved thermal management capability, ACS Nano 13 (2018) 337–345.

[11] G. Zeng, J. Zhao, C. Feng, D. Chen, Y. Meng, B. Boateng, N. Lu, W. He, Flame-retardant bilayer separator with multifaceted van der Waals interaction for lithium-ion batteries, ACS Appl. Mater. Interfaces 11 (2019) 26402–26411.

[12] J. Dai, C. Shi, C. Li, X. Shen, L. Peng, D. Wu, D. Sun, P. Zhang, J. Zhao, A rational design of separator with substantially enhanced thermal features for lithium-ion batteries by the polydopamine–ceramic composite modification of polyolefin membranes, Energy Environ. Sci. 9 (2016) 3252–3261.

[13] S. Wang, P. Takyi-Aninakwa, S. Jin, C. Yu, C. Fernandez, D.-I. Stroe, An improved feedforward-long short-term memory modeling method for the whole-life-cycle state of charge prediction of lithium-ion batteries considering current-voltage-temperature variation, Energy 254 (2022), 124224.

[14] Y. Li, H. Pu, Y. Wei, Polypropylene/polyethylene multilayer separators with enhanced thermal stability for lithium-ion battery via multilayer coextrusion, Electrochim. Acta 264 (2018) 140–149.

[15] C. Shi, P. Zhang, S. Huang, X. He, P. Yang, D. Wu, D. Sun, J. Zhao, Functional separator consisted of polyimide nonwoven fabrics and polyethylene coating layer for lithium-ion batteries, J. Power Sources 298 (2015) 158–165.

[16] V. Deimede, C. Elmasides, Separators for lithium-ion batteries: a review on the production processes and recent developments, Energy Technol. 3 (2015) 453–468.

[17] F. Richter, S. Kjelstrup, P.J.S. Vie, O.S. Burheim, Thermal conductivity and internal temperature profiles of Li-ion secondary batteries, J. Power Sources 359 (2017/08/15/2017) 592–600.

[18] Y. Yang, X. Huang, Z. Cao, G. Chen, Thermally conductive separator with hierarchical nano/microstructures for improving thermal management of batteries, Nano Energy 22 (2016/04/01/2016) 301–309.

[19] L. Wei, Z. Lu, F. Cao, L. Zhang, X. Yang, X. Yu, L. Jin, A comprehensive study on thermal conductivity of the lithium-ion battery, Int. J. Energy Res. 44 (2020) 9466–9478.

[20] R. Liu, J. Chen, J. Xun, K. Jiao, Q. Du, Numerical investigation of thermal behaviors in lithium-ion battery stack discharge, Appl. Energy 132 (2014) 288–297.

[21] G. Guo, B. Long, B. Cheng, S. Zhou, P. Xu, B. Cao, Three-dimensional thermal finite element modeling of lithium-ion battery in thermal abuse application, J. Power Sources 195 (2010) 2393–2398.

[22] V. Vishwakarma, A. Jain, Measurement of in-plane thermal conductivity and heat capacity of separator in Li-ion cells using a transient DC heating method, J. Power Sources 272 (2014) 378–385.

[23] P. Taheri, M. Bahrami, Temperature rise in prismatic polymer lithium-ion batteries: an analytic approach, SAE Int. J. Passeng. Cars-Electron. Electr. Syst 5 (2012) 164–176.

[24] S. Chen, C. Wan, Y. Wang, Thermal analysis of lithium-ion batteries, J. Power Sources 140 (2005) 111–124.

[25] J. Guo, X. Wang, T. Wang, Thermal characterization of microscale conductive and nonconductive wires using transient electrothermal technique, J. Appl. Phys. 101 (2007), 063537.

[26] M. Rahbar, M. Han, S. Xu, H. Zobeiri, X. Wang, Development of differential thermal resistance method for thermal conductivity measurement down to microscale, Int. J. Heat Mass Tran. 202 (2023/03/01/2023), 123712.

[27] P. Pal, Chapter 5 - arsenic removal by membrane distillation, in: P. Pal (Ed.), Groundwater Arsenic Remediation, Butterworth-Heinemann, 2015, pp. 179–270.

[28] B. Zhu, R. Wang, S. Harrison, K. Williams, R. Goduguchinta, J. Schneiter, J. Pegna, E. Vaaler, X. Wang, Thermal conductivity of SiC microwires: effect of temperature and structural domain size uncovered by 0 K limit phonon scattering, Ceram. Int. 44 (2018/07/01/2018) 11218–11224.

[29] H. Lin, S. Xu, X. Wang, N. Mei, Thermal and electrical conduction in ultrathin metallic films: 7 nm down to sub-nanometer thickness, Small 9 (2013) 2585–2594.

[30] J. Liu, T. Wang, S. Xu, P. Yuan, X. Xu, X. Wang, Thermal conductivity of giant mono-to few-layered CVD graphene supported on an organic substrate, Nanoscale 8 (2016) 10298–10309.

[31] B. Zhu, J. Liu, T. Wang, M. Han, S. Valloppilly, S. Xu, X. Wang, Novel polyethylene fibers of very high thermal conductivity enabled by amorphous restructuring, ACS Omega 2 (2017/07/31 2017) 3931–3944.

[32] N. Hunter, A. Karamati, Y. Xie, H. Lin, X. Wang, Laser photoreduction of graphene aerogel microfibers: dynamic electrical and thermal behaviors, ChemPhysChem (2022) e202200417.

[33] A. Karamati, N. Hunter, H. Lin, H. Zobeiri, S. Xu, X. Wang, Strong linearity and effect of laser heating location in transient photo/electrothermal characterization of micro/nanoscale wires, Int. J. Heat Mass Tran. 198 (2022), 123393.

[34] J. Liu, Z. Xu, Z. Cheng, S. Xu, X. Wang, Thermal conductivity of ultrahigh molecular weight polyethylene crystal: defect effect uncovered by 0 K limit phonon diffusion, ACS Appl. Mater. Interfaces 7 (2015) 27279–27288.

[35] H.-S. Yang, M. Wolcott, H.-S. Kim, H.-J. Kim, Thermal properties of lignocellulosic filler-thermoplastic polymer bio-composites, J. Therm. Anal. Calorim. 82 (2005) 157–160.

[36] M. Ivashchenko, A. Opanasyuk, I. Buryk, V. Lutsenko, A. Shevchenko, Optical properties of pure and Eu doped ZnSe films deposited by CSVS technique, J. Nano Electron. Phys. 9 (2017), 1011-1.

[37] G. Rusu, M. Diciu, C. Pirghie, E. Popa, Structural characterization and optical properties of ZnSe thin films, Appl. Surf. Sci. 253 (2007) 9500–9505.

[38] A. Patterson, The Scherrer formula for X-ray particle size determination, Phys. Rev. 56 (1939) 978.

[39] C. Maier, T. Calafut, Polypropylene: the Definitive User's Guide and Databook, Elsevier Science, 1998.

[40] C. Choy, D. Greig, The low temperature thermal conductivity of isotropic and oriented polymers, J. Phys. C Solid State Phys. 10 (1977) 521.

[41] G. Liu, S. Xu, T.T. Cao, H. Lin, X. Tang, Y.Q. Zhang, X. Wang, Thermally induced increase in energy transport capacity of silkworm silks, Biopolymers 101 (2014) 1029–1037.

[42] R. B. Bird, W. E. Stewai, and E. N. Lightfoot, "Phenomena Second Edition.".

[43] S. Franz, B. Friedrich, K. Martin, Emissivity factor of thermoplastic materials for a robot bending process, Ann. DAAAM Proc. 27 (2016).

[44] F.P. Incropera, D.P. DeWitt, T.L. Bergman, Fundamentals of Heat and Mass Transfer, John Wiley, Hoboken, NJ, 2007.

[45] H. Lin, S. Xu, Y.-Q. Zhang, X. Wang, Electron transport and bulk-like behavior of Wiedemann–Franz law for sub-7 nm-thin iridium films on silkworm silk, ACS Appl. Mater. Interfaces 6 (2014) 11341–11347.

[46] W. Jones, H. Norman, March. Theoretical Solid State Physics, Volume 1: Perfect Lattices in Equilibrium, Dover Publications, Mineola, 1985.

[47] G. Kumar, G. Prasad, R. Pohl, Experimental determinations of the Lorenz number, J. Mater. Sci. 28 (1993) 4261–4272.